

CHROMOSPHERIC DIAGNOSIS WITH Ca II LINES: FORWARD MODELING IN FORWARD SCATTERING. I

E. S. CARLIN¹ AND A. ASENSIO RAMOS^{2,3}

¹ Istituto Ricerche Solari Locarno, 6600, Locarno, Switzerland; escarlin@irsol.es

² Instituto de Astrofísica de Canarias, 38205, La Laguna, Tenerife, Spain

³ Departamento de Astrofísica, Facultad de Física, Universidad de La Laguna, Tenerife, Spain
Received 2014 September 29; accepted 2014 December 16; published 2015 February 26

ABSTRACT

This paper presents a synthetic tomography of the quiet solar chromosphere formed by spatial maps of scattering polarization. It has been calculated for the Ca II 8498, 8542, and 3934 Å lines by solving the non-LTE radiative transfer problem of the second kind in a three-dimensional atmosphere model obtained from realistic magneto-hydrodynamical simulations. Our investigation focuses on the linear polarization signals induced by kinematics, radiation field anisotropy, and the Hanle effect in forward-scattering geometry. Thus, instead of considering slit profiles at the limb as normally done in the study of the second solar spectrum, we synthesize and analyze spatial maps of polarization at the disk center. This allows us to understand the spatial signatures of dynamics and magnetic field in the linear polarization in order to discriminate them observationally. Our results suggest some ideas for chromospheric diagnosis that will be developed throughout a series of papers. In particular, Hanle polarity inversion lines and dynamic Hanle diagrams are two concepts introduced in the present work. We find that chromospheric dynamics and magnetic field topology create spatial polarization fingerprints that trace the dynamic situation of the plasma and the magnetic field. This allows us to reconstruct the magnetic field intensity in the middle chromosphere using Stokes V along grooves of null linear polarization. We finally address the problems of diagnosing Hanle saturation and kinematic amplification of scattering signals using Hanle diagrams.

Key words: polarization – radiation: dynamics – radiative transfer – scattering – Sun: chromosphere – Sun: magnetic fields

1. INTRODUCTION

When the line of sight (LOS) points to the solar disk center, i.e., in forward-scattering geometry, the Hanle effect can create linear polarization (LP) in the presence of magnetic fields (Trujillo Bueno 2003b). Namely, a resolved magnetic field that is inclined with respect to the solar radial produces a (“right–left”) symmetry breaking in the scattering process, and thus creates Q and U signals quantifying the magnetic state of the plasma. As in a general case, these signals strongly react to vertical variations of the radiation field anisotropy (“up–down” symmetry breakings). Hence, they also contain unique footprints of the dynamic state of the atmosphere because the radiation anisotropy is highly sensitive to it. Indeed, they are expected to be largely modulated by vertical gradients of temperature and velocity (Carlin et al. 2013). This is important in spectral line polarization forming in non-LTE conditions because in such a case the atomic polarization is strongly coupled with the radiation field, which is Doppler-shifted by the velocity field. On this basis we seek to understand the behavior of the LP signals emerging in forward-scattering geometry from the strongly dynamic and weakly magnetized external layers of the Sun.

Currently, the interest in using the forward-scattering Hanle effect for magnetic field diagnosis is recent and not yet exploited. Early reports were given by Trujillo Bueno et al. (2002) and Stenflo (2003) on chromospheric observations of He I 10830 Å and Ca I 4227 Å, respectively. Lately, Anusha et al. (2011) modeled the polarization of Ca I 4227 Å for explaining some of the observations performed by Bianda et al. (2011) near disk center. In this paper, we investigate the disk center polarization in the Ca II IR triplet lines and in the cores

of the corresponding K line, considering kinematics as an indispensable new ingredient for modeling it.

We adopt complete redistribution in frequencies (CRD) as a good approximation for synthesizing the non-resonant Ca II IR triplet lines (8498, 8542, 8662 Å) and also the core (especially the central six Doppler widths) of the UV 3969 and 3934 Å lines because such wavelengths are strongly affected by Doppler redistribution in the observer reference frame (Uitenbroek 1989; Mihalas 1978). Moreover, when the LOS approaches the disk center, the increasing symmetry in the scattering cancels out partial redistribution (PRD) effects that dominated the linearly polarized spectral wings in the Ca II H and K lines toward the limb (Stenflo 2006). This observational fact reinforces our CRD treatment and a line-core-based diagnosis.

Another key point for describing the line-core polarization is the saturation of the Hanle effect, by which a sufficiently strong magnetic field nullifies quantum coherences in a quantization axis chosen along the magnetic field (i.e., in the magnetic field reference frame). This produces Stokes Q and U that are insensitive to the magnetic field strength, so extending the applicability of the Hanle effect to the inference of the magnetic field orientation. For a transition with a polarizable upper level, Hanle saturation occurs when the effective Larmor frequency is a few times the spontaneous emission rate A_{ul} defining the energy level uncertainty. Thus, as the Zeeman splitting is the Larmor frequency in wavelength units, the Hanle signals appear and saturate as soon as the Zeeman splitting is a few times the *natural* width of the level (Landi Degl’Innocenti & Landolfi 2004, Section 5.16). Furthermore, as weak fields give small splittings in relation to the chromospheric *thermal* line widths, the transversal-Zeeman signals are still negligible and the LP remains controlled by scattering processes (Landi Degl’Innocenti & Landi Degl’Innocenti 1973; Jefferies et al.

1989). That is why the Hanle effect can be saturated with weak fields and why scattering polarization signals are essential for studying weakly magnetized plasmas.

For the Ca II IR triplet lines and the model chromosphere considered here the magnetic field is weak enough for the Hanle effect to be dominant, but strong enough to push it into saturation. This is also the most probable situation in the quiet solar chromosphere (Manso Sainz & Trujillo Bueno 2010). The predominance of the Hanle effect is stronger in non-resonant chromospheric lines such as Ca II 8542 and 8662 Å because their absorption in Q and U originates completely in middle chromosphere layers, where the magnetic field intensity is reduced in comparison to lower layers. The idea is also valid in the core of resonant lines such as the Ca II H and K lines because it forms in the even less magnetized upper chromosphere. Although in these cases the Hanle effect clearly dominates the quiet Sun line cores, the linear polarization is in general a non-linear superposition of Hanle and Zeeman effects along wavelength.

On the contrary, the circular polarization is fundamentally described by the longitudinal Zeeman effect (wavelength splitting due to the magnetic field component along the LOS). Hence, we have followed here the usual approach of disregarding the small contribution of the atomic polarization to Stokes V in order to also calculate circular polarization maps. Stokes V in the Ca II 8542 and 8662 Å lines has an especially good sensitivity for diagnosing longitudinal magnetic fields (e.g., Socas-Navarro et al. 2006).

We emphasize that the traditional modeling of scattering polarization signals and Hanle effect has always been performed while neglecting macroscopic velocities and considering only one spatial direction (a slit) at the solar limb. Although this is enough for understanding essential features of the second solar spectrum (e.g., Stenflo & Keller 1997), it appears questionable for a true diagnosis of chromospheric signals. On one hand, the vertical velocity gradients are not only able to destroy LP in particular situations but also can boost the LP amplitudes up to more than one order of magnitude in relation to the static case (Carlin et al. 2013). This becomes crucial for measuring chromospheric magnetic fields and for correctly reproducing the observed linear polarization profiles. On the other hand, the approach typically followed to synthesize scattering polarization is incompatible with using state-of-the-art MHD models, where dynamics and spatial extension are essential. The technical asynchrony between both fields of research is partially due to intrinsic difficulties found in the theoretical (Bommier 1997; Casini et al. 2014) and numerical (Trujillo Bueno & Manso Sainz 1999; Anusha & Nagendra 2011) aspects of the scattering polarization. The numerical situation worsens when considering the abrupt velocity gradients in the rarified solar chromosphere because of the relation between opacity inhomogeneities induced by Doppler shifts along a given ray and the (lack of) convergence to a joint solution for the rate and transfer equations (Mihalas 1978).

We address the above issues by solving the radiative transfer (RT) with polarization in a radiation three-dimensional (3D) MHD model, considering each vertical as a plane-parallel atmosphere but using the corresponding atomic populations computed in three dimensions by Leenaarts et al. (2009). Hence, the resulting chromospheric polarization maps are driven by the Hanle effect and vertical variations in all the physical quantities. The method is reasonable because, in the chromosphere, the atomic polarization is dominated by enhancements of radiation

field anisotropy due to vertical gradients of density, temperature, and velocity, and not by the inhomogeneous horizontal illumination, which is azimuthally isotropized by large photon mean-free paths and random short-scale intensity distributions throughout the horizontal plane. The possible limitations of such an assumption are compensated with the reduced requirements in time and computational resources with respect to the 3D polarized-RT codes starting to emerge right now (Anusha & Nagendra 2011; Štěpán & Trujillo Bueno 2013). We can thus offer a precedent to test the reliability of non-full-3D RT codes with atomic polarization while simultaneously investigating diagnosis strategies that require a detailed analysis of the physical situation in the models.

2. TECHNICAL DETAILS ABOUT THE CALCULATIONS

The atmospheric model considered is a snapshot of a radiation MHD simulation of the solar atmosphere computed by Leenaarts et al. (2009) with the Oslo Stagger Code (Hansteen et al. 2007). This code solves the set of MHD equations that describe the plasma motion together with the RT equation. It employs an LTE equation of state and includes non-LTE radiative cooling in the corona and upper chromosphere, also considering thermal conduction along magnetic field lines. The electron density was computed assuming LTE ionization for all relevant species. Photoionization by hydrogen Lyman lines was not taken into account.

The snapshot has $256 \times 128 \times 213$ grid points and a physical size of $16.6 \times 8.3 \times 5.3$ Mm. For our aims, we selected a volume⁴ with $5.85 \times 5.98 \times 4$ Mm ($91 \times 93 \times 191$ grid points). The snapshot has a mean magnetic field strength of 120 G at 300 Km, which is representative of the magnetization expected in quiet regions of the solar photosphere (Trujillo Bueno et al. 2004; Asensio Ramos 2014). The hydrogen number density was not available in the supplied model. To compute it, we considered the stratifications of temperature, density, and electron number density and we solved the chemical equilibrium and ionization equations for all the relevant atomic species, including hydrogen, as explained in Asensio Ramos (2004). The synthesis of polarization produced only by the Zeeman effect in similar atmospheric models has been presented by De la Cruz Rodríguez et al. (2012).

We used the corresponding 3D NLTE Ca II level populations provided by Leenaarts et al. (2009) as inputs to solve the RT problem of the second kind described in Landi Degl'Innocenti & Landolfi (2004), which results from considering atomic polarization and the Hanle effect. Namely, it implies solving the RT equations for the Stokes vector together with the statistical equilibrium equations (SEE) for the multipolar tensor components of the atomic density matrix $\rho_O^K(J)$ (with $K = 0, \dots, 2J$ and $-K \leq Q \leq K$) in each energy level J . Thus, the atomic level populations ($\propto \rho_O^0(J)$) that were calculated with 3D RT for each level are iteratively redistributed among the corresponding magnetic energy sublevels. Essentially, it gives rise to the alignment terms $\rho_O^2(J)$, sourced by the radiation field anisotropy in the SEE, and to the quantum coherences $\rho_Q^2(J)$ (with $Q \neq 0$), which can be created and destroyed by the magnetic field through the so-called magnetic kernel in the SEE (Hanle effect).

⁴ The portion chosen from the data cube found in Leenaarts et al. (2009) spans from 0 to 5.85 Mm in the x direction, from 1 to 6.98 Mm in the y direction and from -0.5 to 3.5 Mm along the vertical.

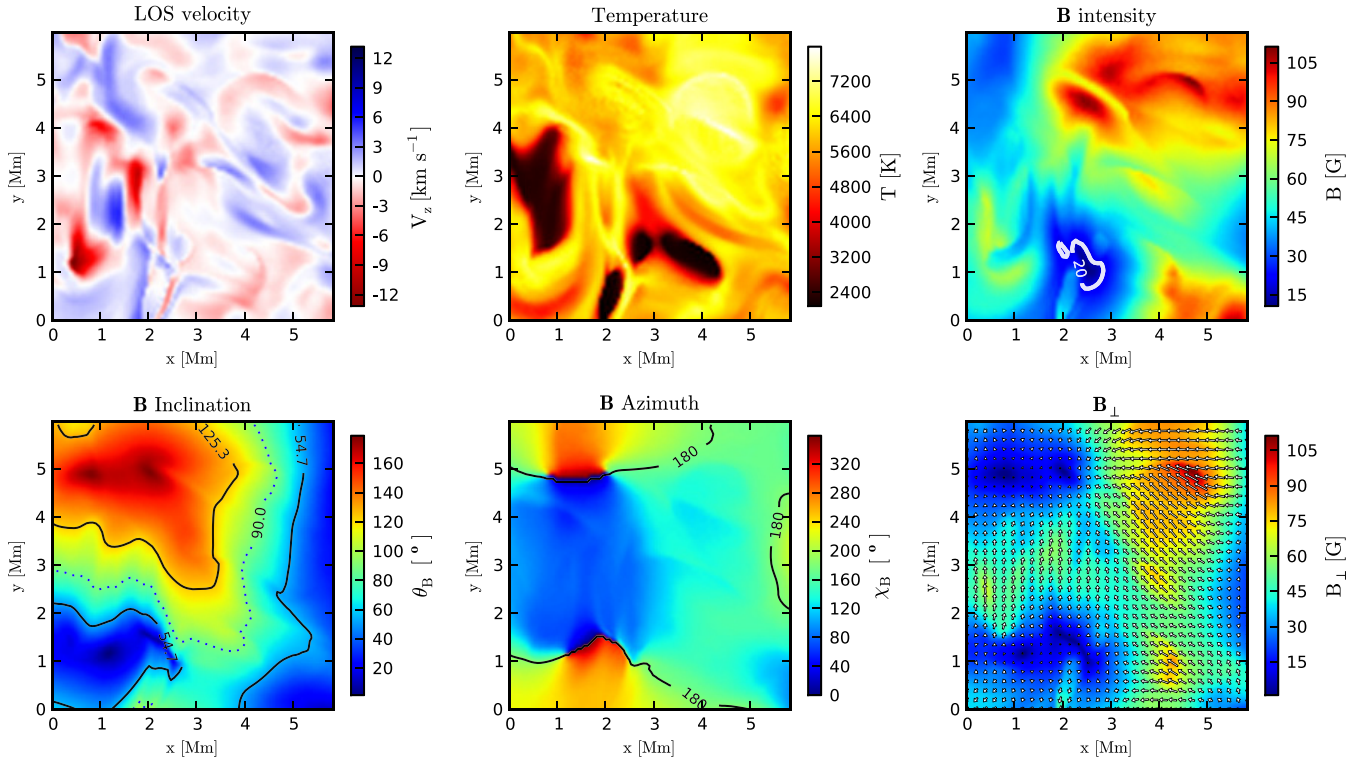


Figure 1. Physical quantities at $\tau_{v_0} = 1$ for the 8542 Å line. Upper: vertical velocity, temperature, and magnetic field intensity. Lower: magnetic field inclination, magnetic field azimuth, and horizontal magnetic field (intensity and vector).

The Hanle effect is also contained in the RT coefficients. Emissivities, absorptions and magneto-optical terms are the same as in Manso Sainz & Trujillo Bueno (2010) but including the action of macroscopic motions. Although using populations obtained with 3D RT, we performed the RT of the Stokes vector treating each model column as an independent plane-parallel atmosphere, hence neglecting the effect of horizontal inhomogeneities in the plasma. Furthermore, we took into account that in weak magnetic fields, Stokes V is due to the longitudinal Zeeman effect while Stokes Q and U are due to scattering and Hanle polarization, the linear signals of the transverse Zeeman effect being a second-order contribution. In that case the RT equations for Stokes Q and U can be decoupled from the RT equation for Stokes V . This approach is excellent for modeling the polarization in the quiet Sun, where $B \lesssim 100$ G. Following it, we obtained the linear polarization in the Hanle regime and the circular polarization in the Zeeman regime.

Lorentz damping rates and inelastic collisional rates were taken from Shine & Linsky (1974). Depolarizing elastic collisions with neutral hydrogen and collisional alignment transfer rates were taken from Derouich et al. (2007). A more detailed description of our synthesis computer code is presented in the Appendix. Previous applications of a similar code can be found in Carlin et al. (2013) and in the references therein.

The selected data cube contains 8463 columns or vertical models, each one corresponding to a pixel in the maps. In order to decrease the computational load, we eliminated the unnecessary points along the vertical direction by adaptively truncating columns in height. For each column, we estimated the heights where $\tau_{\text{cont}}^{8498} = 10^3$ (setting the lower boundary position) and $\tau_{v_0}^{\text{Kline}} = 10^{-4}$ (setting the upper boundary position). Thus, we run the RT calculations with less grid points but without appreciable loss of accuracy in the obtention of the density

matrix elements and the Stokes vector. In other words, the boundary conditions (sufficiently optically thin outside and sufficiently optically thick inside) are still fulfilled for all of the spectral lines. To find the vertical limits commented above we obtained the iso-surfaces of optical depth by calculating, for each transition and each vertical of the data cube, the optical depth ($\tau_{v_0} = -\int \eta_I(z, v_0) dz$) at line center along rays with $\mu = 1$. The absorption coefficient is approximated as $\eta_I \approx \eta_I^{\text{cont}} + (hv/4\pi)B_{lu}N_\ell(1/\sqrt{\pi}\Delta v_D)$, where η_I^{cont} is the absorption coefficient for the continuum and the second addend is the line absorption coefficient at line center. N_ℓ is the overall lower level population of the considered transition, B_{lu} is the Einstein coefficient for absorption, and Δv_D is the thermal width of the line profile. This calculation is also needed to evaluate the physical magnitudes at several optical depths, especially at the main formation heights around $\tau_{v_0} = 1$, which is useful to analyze the results of the synthesis. Examples of maps at $\tau_{v_0} = 1$ for the Ca II 8542 Å line are shown in Figure 1. The corresponding heights at optical depth unity are drawn in Figure A1, in the Appendix.

The pixels having a chromospheric magnetic field that is predominantly horizontal define what we call *Horizontal Field* (HF) regions, where $\cos\theta_B < 1/\sqrt{3}$. Thus, HF regions are confined by pixels whose magnetic field lines at $\tau_{v_0} = 1$ have the Van Vleck inclinations,⁵ defined by $\cos\theta_B = 1/\sqrt{3}$ (solid contours in the bottom left panel of Figure 1). HF areas surround the complementary *Vertical Field* (VF) areas, where chromospheric magnetic field vectors are predominantly vertical. We will use this nomenclature in our analysis.

⁵ Such inclinations virtually separate vertical from horizontal rays at each point and appear related to quantities describing the scattering polarization (e.g., radiation field anisotropy, spherical tensors for polarimetry, or equations in next section).

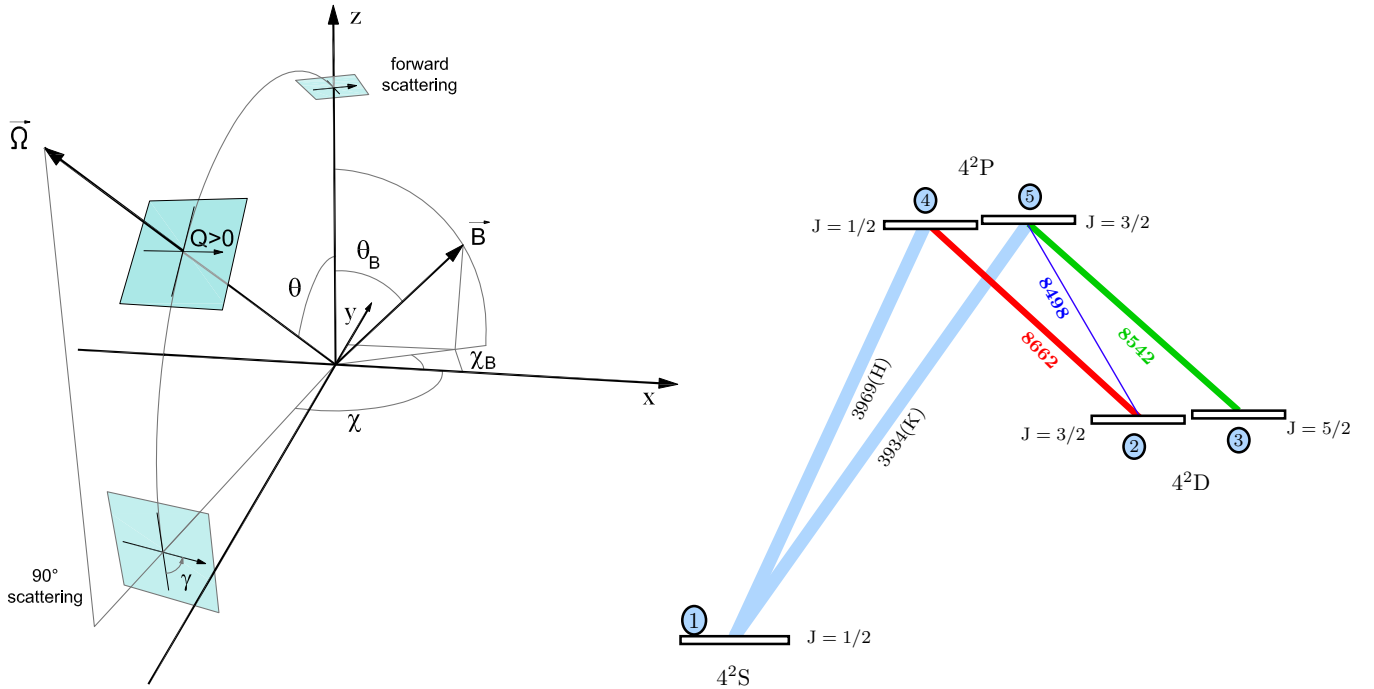


Figure 2. Left: atmospheric reference frame. The angles χ , θ , and γ define the LOS $\bar{\Omega}$ and are negative/positive in the counter/clockwise sense. The green squares represent the corresponding plane of the sky. Right: atomic model considered. Energy levels have been labeled from 1 to 5. A thicker transition line represents a larger spontaneous emission coefficient A_{ul} .

3. FORWARD-SCATTERING HANLE EFFECT IN SATURATION

The critical Hanle field of an atomic level is the magnetic field strength around which the variability in the atomic polarization due to interferences (quantum coherences) between the corresponding magnetic energy sublevels is maximized. For instance, in the upper level of a two-level atom this occurs with a critical field $B_H \sim A_{ul}/(1.4 \times 10^{-6} g_L)$, g_L being the Lande factor. However, in the Ca II IR triplet lines synthesized here, the linear polarization is in the *saturated Hanle regime* because the chromospheric magnetic field is significantly stronger than the corresponding critical Hanle fields ($B \gtrsim 5B_H$). Considering Hanle saturation in Equations (7.16) of Landi Degl'Innocenti & Landolfi (2004) and estimating the linear polarization in the Eddington-Barbier approximation (Trujillo Bueno 2003a), we have obtained the following analytical expressions that describe the line-center forward-scattering polarization and that help us understand our results. They can be applied to non-blended and sufficiently strong spectral lines forming in the weak-field and weak-anisotropy regime found in quiet stellar chromospheres:

$$\frac{Q}{I} \simeq -\frac{3}{4\sqrt{2}} \cdot \sin^2 \theta_B \cdot (3 \cos^2 \theta_B - 1) \cos(2\chi_B) \cdot \mathcal{F} \quad (1a)$$

$$\frac{U}{I} \simeq -\frac{3}{4\sqrt{2}} \cdot \sin^2 \theta_B \cdot (3 \cos^2 \theta_B - 1) \sin(2\chi_B) \cdot \mathcal{F}. \quad (1b)$$

All the terms in the rhs of Equations (1) have to be evaluated at $\tau_{v_0}^{\text{LOS}} = 1$, with⁶ $\mathcal{F} = \omega_{J_u J_\ell}^{(2)} \sigma_0^2(J_u) - \omega_{J_\ell J_u}^{(2)} \sigma_0^2(J_\ell)$ being the non-magnetic contribution of the fractional atomic alignment ($\sigma_0^2 = \rho_0^2/\rho_0^0$) generated in the levels of the transition. We

⁶ We follow the standard notation for the upper and lower level atomic quantum numbers ($\alpha_u J_u$ and $\alpha_\ell J_\ell$) and the polarizability coefficients $\omega_{J_u J_\ell}^{(K)}$ weighting the atomic polarization (Landi Degl'Innocenti 1984).

often call \mathcal{F} the thermodynamical factor because the anisotropy and the atomic alignments modulating it indirectly depend on kinematics and thermodynamics. The angles χ_B and θ_B are the azimuth and inclination of the magnetic field vector in the reference system shown in Figure 2. The LOS $\bar{\Omega}$ is defined by the angles $(\chi, \theta) = (-\pi/2, 0)$ in that figure. Thus, in all our maps the direction of positive polarization given by Equations (1) in the plane of the sky is parallel to the x -axis for Q and inclined 45 deg counterclockwise from the x -axis for U .

Equations (1) isolate in \mathcal{F} the effect of the anisotropic illumination while showing that the emergent polarization in the saturation regime of the Hanle effect does not depend on the field strength but only on its orientation. The Hanle effect in forward-scattering produces linearly polarized radiation at maximum along or perpendicular to the projection of the magnetic field vector on the solar surface. Note that in forward-scattering both Stokes parameters are essentially equivalent in their physical dependencies and have the same maximum and minimum values. This does not occur in other lines of sight. Note also that the axial symmetry around the solar radial (that is, a vertical magnetic field) nullifies the forward-scattering polarization.

4. SYNTHETIC POLARIZATION IN FORWARD-SCATTERING

4.1. Slit Profiles

We have analyzed qualitatively the synthetic Stokes profiles at 8542 Å along two fictitious spectrograph slits (Figure 3) while inspecting the physical situation of the atmosphere in each point.

First, we note that several intensity spectra in the selected slits show brightenings in the wings and/or in the core.

On one hand, similar increased emission in both wings of 8542 Å is also reported in solar observations (Reardon et al. 2013). In our results, it is associated with photospheric heating, which, at least in the shown profiles, also correlates with

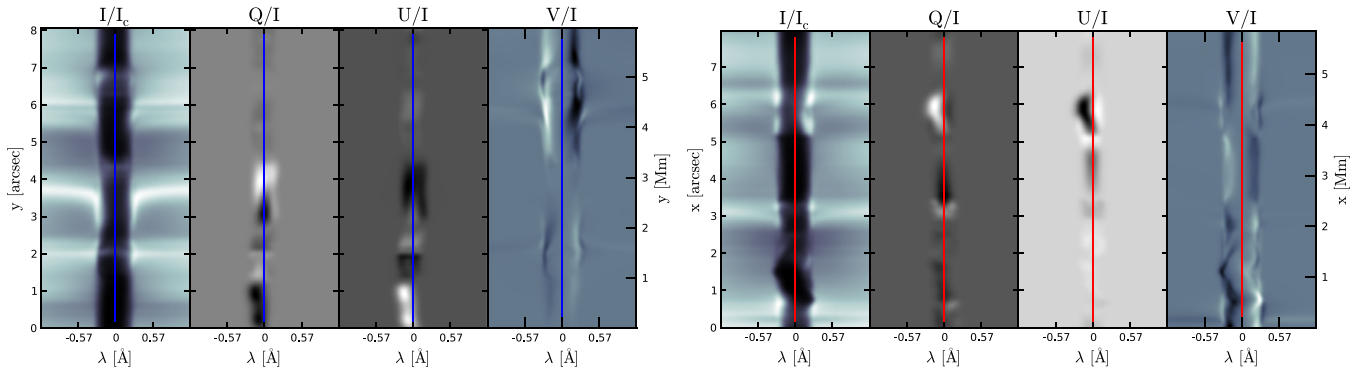


Figure 3. Examples of synthetic Stokes profiles at two simulated spectrograph slits. Left panel: blue slit: placed vertically at $x = 2$ Mm. Right panel: red slit: placed horizontally at $y = 2$ Mm. The left panel is analyzed in the text. Note the two different spatial scales.

photospheric compression: the downward plasma is compressing sub-chromospheric layers while the low chromosphere and minimum temperature region are almost at rest. This situation sometimes coincides with a photospheric bright point in the models. In such cases, the magnetic field is more intense and almost vertical in low layers, which produces significant Stokes V signals. That is the case at $y \sim 2''$ and $y \sim 6''$ in the blue slit.

In pixels where the temperature gradient at the low chromosphere is high enough, we can also appreciate reversal peaks enclosing the intensity line-core (blue slit, $y \sim 3''$) that are not necessarily correlated with wing/core emissions. These features resemble the K2 and H2 reversals of the solar H and K lines (Linsky & Avrett 1970) forming at the top chromospheric layers in the Sun, but, to our knowledge, do not appear in solar observations of the 8542 and 8662 Å lines. Such discrepancy can indicate a lack of temporal and spatial resolution in observations and/or a lack of realistic temperature stratification, resolution, or small-scale dynamics in the models. At least the latter option is in principle a known issue pointed out by Leenaarts et al. (2009). We note that introducing a height-dependent microturbulent velocity there where the source function decouples from the Planck function, the intensity emerging from near layers can be mixed and the reversals can be effectively suppressed. A more realistic model thermal stratification can be obtained by accounting for other heating mechanisms (Khomenko & Collados 2012; Martínez-Sykora et al. 2012).

On the other hand, the weaker brightenings appearing in the intensity line core (sometimes observed and cataloged as raised-core profiles; see e.g., de la Cruz Rodríguez et al. 2013) are related to small localized increments of temperature (chromospheric heatings) in the mid-upper chromosphere (e.g., blue slit at $y \sim 4''/3$). In cases with stronger temperature bumps in the formation region or with significant temperature gradients between the temperature minimum and the line formation region, the brightenings are larger and the intensity profiles are in emission (not shown here). Similar self-reversals are known to exist in the solar chromosphere (e.g., Pietarila et al. 2007; Judge et al. 2010).

Velocity gradients during atmospheric expansion/compression create Doppler radiative uncouplings between lower and mid-upper chromosphere that also rise the line-core intensity (Doppler brightenings). They are sources of increased Q and U signals because the radiation field becomes more anisotropic than in a static case, so the atomic polarization is larger (Carlin et al. 2012). If the velocity gradient is formed by a chromospheric shock wave, local heatings are present and also produce brightenings in intensity. But this connection seems to

disappear in cool expanded chromospheres. Furthermore, the scattering polarization at the disk center tends to zero inside the VF region because the reduced magnetic field inclination diminishes the Hanle effect. Thus, a relatively cool or expanded chromosphere, and/or the modulation produced by the magnetic field, explains that a brightening in the intensity line core is not always correlated with larger LP signals.

Examples of LP signals enhanced by vertical velocities are shown around $y \sim 1''$ and $y \sim 4''$ in the blue-slit panel. The essential difference between them is that $y \sim 4''$ corresponds to a compressive atmosphere and $y \sim 1''$ corresponds to an expansive one. Although the latter case is generally less efficient in increasing the anisotropy of the radiation field, both positions have similar LP amplitudes in this snapshot because of a larger velocity (gradient) at the chromosphere of $y \sim 1''$. In both slit positions the longitudinal magnetic field strength is very weak in the chromosphere ($\lesssim 50$ G) but also in the upper photosphere, which explains the absence of circular polarization.

Scattering linear polarization signals with significant asymmetries but small Doppler shifts (e.g., Stokes Q at $y \sim 3''/8$) occur in the presence of steep velocity gradients but low velocities in the chromosphere ($\lesssim 3$ km s $^{-1}$). To the contrary, significant Doppler shifts and near-symmetric profiles can happen (e.g., $y \sim 1''$) when chromospheric velocities do not change their sign along the vertical but do change the sign of their gradients (typical of expansive atmospheres driven by shocks). In general, the asymmetries are produced because the Doppler shifts along the LOS change the formation heights and the optical properties of the medium at different wavelengths. However, in the case of the LP profiles, such RT effects are actually powered by the major contribution coming from the anisotropic illumination, which increases the vertical gradient of atomic alignments. In other words, vertical gradients of anisotropy are being translated to asymmetries along wavelength, which can easily surpass the asymmetries produced by motions along the LOS (Carlin et al. 2013). Asymmetries in Stokes V and I (e.g., Martínez Pillet et al. 1990) are not analyzed here but naturally are also present in our results.

Several of the above-mentioned features appear together in the blue-slit panel of Figure 3 around $y \sim 2''$. As commented before, it corresponds to a region over a bright point. The physical situation here is very different between the lower and the upper layers. We see reversal peaks as well as intensity brightenings in the core and the wings. Accordingly, the atmospheric analysis shows a photospheric heating by compression (downward velocities below the temperature minimum) but upward velocities in the chromosphere, which produces a

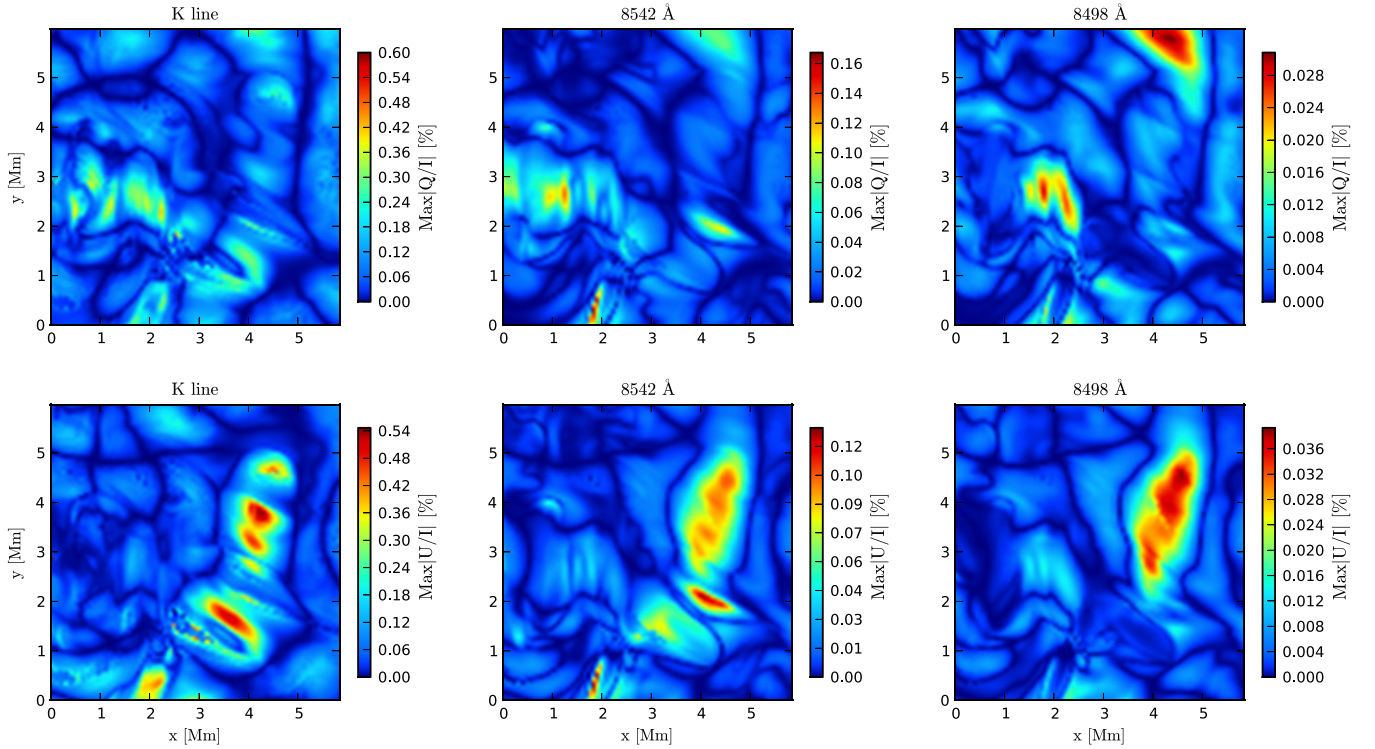


Figure 4. Synthetic maps of maximum fractional polarization in Q and U for 8498 Å (right panels), 8542 Å (middle panels), and 3934 Å (K line, in the left panels).

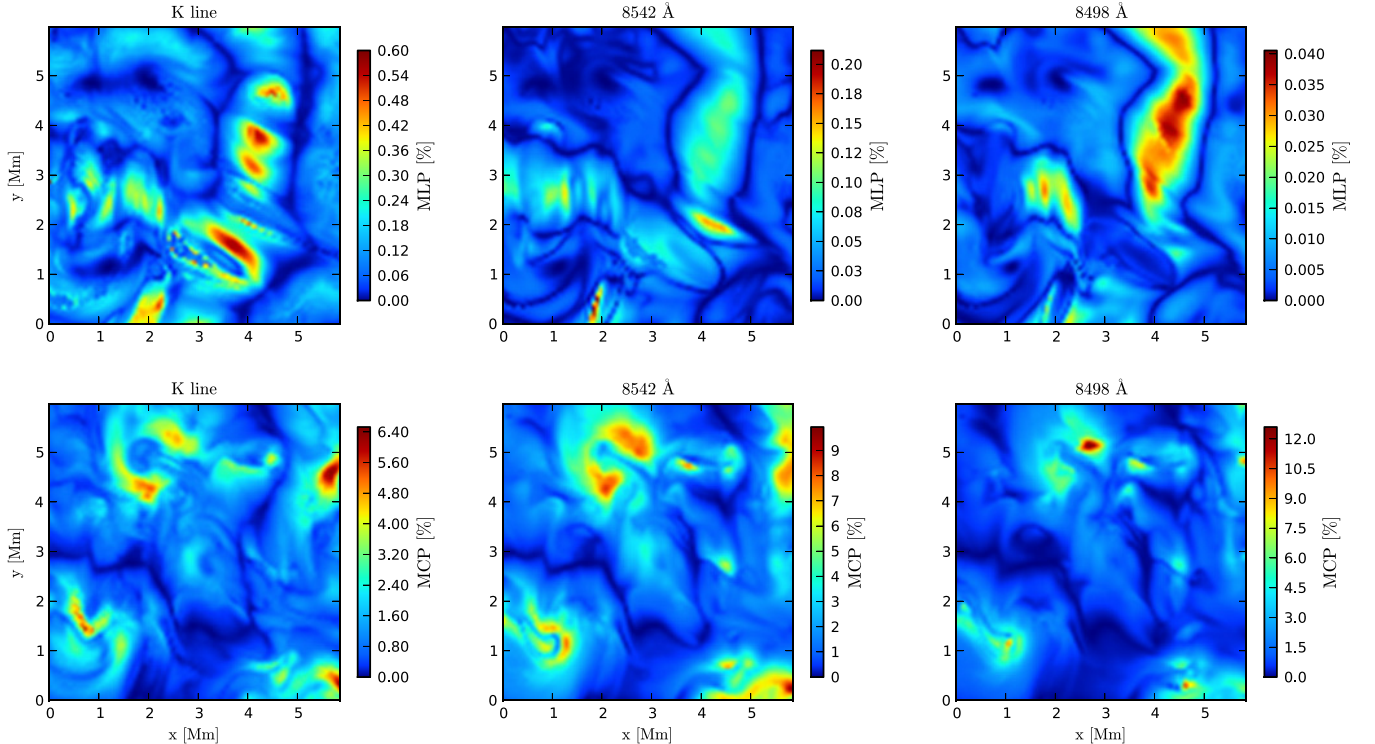


Figure 5. Synthetic maps of linear and circular polarization for 8498 Å (right panels), 8542 Å (middle panels), and 3934 Å (K line, in the left panels). Top panels: maximum linear polarization amplitudes calculated as $MLP = \sqrt{\text{Max}|Q/I|^2 + \text{Max}|U/I|^2}$. Bottom panels: maximum of the absolute value of the fractional circular polarization (MCP).

significant gradient between both layers. The Hanle signal in Stokes Q and U is weak because the chromospheric magnetic field vector is near vertical but is not zero because its inclination changes significantly along height in the formation region (twisted magnetic field in the surroundings). A relatively

strong *vertical* magnetic field at the *photosphere* and around the temperature minimum is producing a notable Stokes V signal, although the chromospheric field strength is weak.

Note that the response functions to magnetic field strength in Stokes V at 8542 Å are expected to be maximum in wavelengths

associated with the Stokes V peaks and in the bottom chromosphere layers (Uitenbroek 2006), while the corresponding scattering polarization signals are forming substantially higher. Then, the vertical magnetic field gradients reproduced in the models give maximum amplitudes in synthetic QU -Hanle and V -Zeeman profiles that correspond to different field strengths.

The changes of sign in Stokes Q and U at $y \sim 1''3$ and $y \sim 2''$ are due to variations in the chromospheric magnetic field azimuth (crosses through zero produced by χ_B in Equations (1)). Similar signatures can be easily seen in many routine observations.

4.2. Polarization Maps

Figure 4 contains maps of maximum scattering polarization for the lines 3934 Å (Ca II K line), 8542 Å, and 8498 Å. The quantities displayed are $100 \cdot \max|Q/I|$ and $100 \cdot \max|U/I|$. When these maps are made in a fixed wavelength (typically the line center) that is different from the one corresponding to the maximum amplitudes, the result is a notable signal fading in pixels where chromospheric velocities are substantial.

In general, the areas of the maps with significant LP always have a notably inclined magnetic field (HF regions). Out of such areas, the LP amplitudes are always below 1/5 of the maximum value in the map.

In many pixels the amplitudes have the same order of magnitude as those calculated by Manso Sainz & Trujillo Bueno (2010) in semi-empirical models, but, where chromospheric velocities⁷ are above $\sim 5 \text{ km s}^{-1}$, we see relative enhancements that reach one order of magnitude in the amplitudes of the 8542 Å and 8662 Å lines with respect to semi-empirical models. This is also true for the 8498 Å line only if the low chromosphere is not too cool because in that case the LP in the 8498 Å line is always insignificant (low-temperature patches in upper middle panel of Figure 1 coincide with areas of almost-zero Q and U). The largest LP amplitudes in this line appear without correlation with large velocities and are twice as large as in the FALC model. Thus, the 8498 Å anisotropy is affected by velocity gradients but seems to be dominated by temperature in these models.

The differences between the Q and U maps are understood with Equations (1). When the magnetic field existing in a region experiences a change in its azimuth, the polarization patches stand out in Q and attenuate in U or vice versa, so just comparing Q and U regions gives us an idea of the approximate directions of the magnetic field. Patches with large Stokes Q and low Stokes U indicate that the field is chiefly oriented along some of the reference axes for Q (vertically or horizontally in the maps). If the opposite holds, the field is then mainly oriented in directions lying at ± 45 deg.

Figure 5 shows the maximum values of the total fractional linear polarization (left panels) and fractional circular polarization (right panels) for the same three spectral lines. Pixels with negligible circular polarization are where the magnetic field is almost horizontal *below* the main formation heights of the corresponding spectral line core. Such pixels are confined in patches with the largest linear polarization.

Patches with the largest linear polarization for the 8498 Å line are also the hottest in the HF region. However, for the 8542 Å line, the largest linear polarization signals are in pixels

with the largest vertical velocity in the HF region. The circular polarization in the 8542 Å line is conspicuously marking the vertical magnetic field concentrations. Empirically, we find that the circular polarization amplitudes in 8542 Å at each pixel are roughly twice the corresponding ones in the K line.

5. HANLE POLARITY INVERSION LINES

5.1. Description

In the maps of Stokes Q and U (Figure 4), we observe lines where the fractional scattering polarization is zero. We call them ‘‘Hanle Polarity Inversion Lines’’ (HPILs) because they are equivalent to the polarity inversion lines of the Zeeman regime. These groove-like structures appear in the polarization maps as a consequence of the weak-field dependences that Q and U display according to Equations (1). Interestingly, the HPILs encode the topology of the magnetic field pervading the solar model. In this work, we restrict their description to the forward-scattering geometry.

We identify three kinds of HPILs produced by three different sources that can act together. To explain them in forward-scattering and Hanle saturation we use Equations (1). Saturation holds easily for the $\lambda 8498$, $\lambda 8542$, and $\lambda 8662$ lines. Then, their Stokes Q and U variations are all described by Equations (1).

The first kind of HPILs is due to the inclination of the magnetic field and is explained by the term $\sin^2\theta_B \times (3 \cos^2\theta_B - 1)$. They appear in the same pixels for Stokes Q and U (hence also in the total linear polarization) because they are independent of the magnetic field azimuth. In the maps they can be found where the magnetic field is mostly vertical as well as in the frontiers of the VF and HF regions (i.e., bordering areas with null longitudinal Zeeman polarization in Stokes V). Namely, they are where $\theta_B = 90 \pm 90^\circ$, $90 \pm 35:27$, as confirmed by Equations (1), and so connect the pixels with such inclinations. As $\theta_B = 90 \pm 35:27$ correspond to a magnetic field forming the Van Vleck angle with the vertical, we call this first type of null polarization lines ‘‘Van Vleck HPILs.’’ As the magnetic field emerges in bipolar structures, the Van Vleck HPILs are continuous lines enclosing the magnetic poles. It is interesting that the mere identification of these lines is an accurate measurement of the field inclination at the main formation height of a spectral line.

The second kind of HPILs is called *azimuthal* because the corresponding spatial features depend on the magnetic field azimuth. An HPIL appearing in a map of Stokes Q (or Stokes U) is of azimuthal type if it does not appear in the same place for Stokes Q as for Stokes U . In pixels defining an azimuthal HPIL in Stokes Q , the magnetic field vector is lying along the positive reference direction for Stokes U ($\pm 45^\circ$ with respect to the x -axis in our maps) or perpendicularly. The pixels defining it in Stokes U have a magnetic field vector lying along the positive reference direction for Stokes Q or perpendicularly. Following an azimuthal HPIL in the maps we connect pixels with the same magnetic field azimuth.⁸ Note also that, when azimuthal HPILs intersect, the cross point must have a magnetic field that is completely vertical (so the cross point is an HPIL of the first kind). Consequently, azimuthal HPILs have a radial nature, beginning in an area of concentration of photospheric magnetic flux and ending in another one.

⁷ In general, we find an association between larger velocities and larger velocity gradients, so we talk indistinctly of one or other quantity.

⁸ In our definition, an azimuthal HPIL always begins and ends in an intersection of azimuthal HPILs. Thus, after such an intersection, the continuation of the null line is always another azimuthal HPIL that can correspond to another azimuth.

Finally, a third possible origin of HPILs is a particular configuration of the anisotropy of the radiation field persisting across a region in the maps. They are *thermodynamically induced* HPILs due to the \mathcal{F} term in Equations (1) and appear at the same time in the Q and U maps for a spectral line, just as the Van-Vleck-type ones, but are independent of the magnetic field inclination. To grasp some idea about the conditions in which they form, note that the thermodynamical HPILs have zero linear polarization because the non-magnetic factor \mathcal{F} in Equations (1) is negligible. Thus, we have

$$\mathcal{F} = \omega_{J_u J_l}^{(2)} \sigma_0^2(J_u) - \omega_{J_l J_u}^{(2)} \sigma_0^2(J_l) = 0. \quad (2)$$

In the simplest case, given by the line 8662 Å, it yields the condition

$$\sigma_0^2(J_2) = \frac{\rho_0^2(J_2)}{\rho_0^0(J_2)} = 0 \quad \text{at} \quad \tau^{8662} = 1 \quad (3)$$

How can such a condition be fulfilled? Let us suppose that we have identified a thermodynamic HPIL appearing at the same time in Q and U maps for the 8662 Å line. Equation (3) is satisfied in that region⁹ when the atomic alignment $\rho_0^2(J_2)$ tends toward zero, or when the overall population ($\propto \rho_0^0(J_2)$) increases too much, or when both things happen at the same time.

A larger level-2 population (see energy levels in Figure 2) can be achieved with an increment of temperature in the top parts of the chromosphere. Such an increment strengthens the Ca II H line intensity emission (forming at the top), which illuminates the lower chromospheric layers from above. This extra illumination arriving at the chromospheric layers immediately below (where the 8662 Å line originates) increases the population pumping from level 1 to level 4, which, in turn, produces an extra population in level 2 by spontaneous emission. Higher temperature thus means more population in higher energy levels (levels 4 and 5) and more emission (at 8662 Å) produced by electrons decaying from level 4 to level 2. Furthermore, if at the same time the formation region of the 8662 Å line is meaningfully cool (after the pass of an upward shock for instance), the absorption of electrons from level 2 to level 4 will decrease (absorption to level 5 can be neglected), and thus the population arriving from level 4 is retained in level 2. As the absorption between level 2 and level 4 is small, the 8662 Å line cannot be polarized because its polarization can only be generated by dichroism (selective absorption; Manso Sainz & Trujillo Bueno 2003a).

On the other hand, to have a negligible alignment in level 2, we need a formation region illuminated with a weak radiation field anisotropy. It is well known that the radiation field anisotropy tends to zero when and where the contribution of the mainly horizontal illumination equals the contribution of the vertical one. In these models, it mainly occurs in pixels that separate areas with a significantly cool formation region from areas where the formation region is relatively hot. If, furthermore, such pixels do not contain significant velocity gradients, the existing low alignment will not be enhanced by kinematics.

The previous situations affecting Equation (3) are all happening in the borders of cool chromospheric plasma bubbles appearing in the atmosphere. In those places, the linear polarization is zero. To examine this, we first identified the location

⁹ In principle, the region associated with a thermodynamical HPIL might not be a line in the map, but we still call it an HPIL for consistency.

of the thermodynamical HPIL in the Stokes maps. Then, with 3D visualizations (see Figure 6 or their stereographic view in Figure A2, in the Appendix), we inspected the thermodynamical stratification of the verticals enclosing the cool bubble. In the interior of the volume, the chromospheric temperature is as cool as 3000 K and the anisotropy is dominated by vertical radiation coming from above the bubble and from the photosphere. On the contrary, the line formation region outside the bubble is significantly hotter. Consequently, the horizontal radiation dominates, changing the sign of the alignment with respect to the interior of the bubble. Thus, by continuity, a line where the net alignment is zero must exist in the middle of both regions (the bubble's "frontier") because it is positive on one side and negative on the other.¹⁰ That is a thermodynamical¹¹ HPIL and it has been induced by spatial differences in the chromospheric dynamic.

A cool bubble is shown around $(x, y) = (3.8, 1.5)$ Mm in the temperature panel of Figure 1. The corresponding HPILs appear in Stokes Q and U maps of the 8542 and 8662 Å lines, surrounding the low-temperature region. For instance, a part of the null line is connecting the points (3.5, 2) and (4.5, 1) Mm. The thermodynamic HPIL can be distinguished from a Van Vleck HPIL because the former is around cool patches and crosses lines of null *circular* polarization.

In the effective Hanle regime (this is, out of saturation), magnetic field dependences different from the ones in Equations (1) can appear to be multiplying the density matrix components in the homologous expressions for Q and U . Thus, the approximated separation between magnetic field orientation and something similar to the thermodynamical factor could not be possible anymore. In such a case, the zeros of the linear polarization at the line center can, in general, follow other analytical expressions, therefore defining new kinds of HPILs or nullifying those already defined here. Only when such analytical dependencies are common for all the multipolar density matrix components the corresponding HPILs would remain valid for any magnetic field regime.

Note that the location, contrast, and width of an HPIL in the polarization maps provide information about the variation with height of the magnetic field along the formation region of the spectral lines. HPILs pertaining to spectral lines forming at different heights have a different appearance because the magnetic field inclination changes with height. This suggests the possibility of deducing the 3D topology of the chromospheric magnetic field from the two-dimensional (2D) maps of the Stokes vector in different spectral lines. A different idea is to make histograms of the mean size of the regions enclosed by the HPILs for characterizing some magnetic field parameter (helicity, inclination, azimuth) in a map. The comparison of scattering polarization footprints between models and high-sensitivity observations would represent a very fine test of our knowledge about the quiet Sun magnetic field.

Today, the practical measurement of these structures sounds very challenging *in the Ca II IR triplet lines*. The visual definition of HPILs in observational maps will depend on the instrumental sensitivity and resolution. Furthermore, diffuse light arriving at the detector can mask the HPILs because it diminishes the contrast between regions with and without polarization.

¹⁰ There is also a correspondence with the velocities. The bubble interior is produced by an expansion cooling down the atmosphere (upward velocities) and the bubble exterior is a contraction (downward velocities). Thus, in the HPIL the velocity is almost zero or insignificant.

¹¹ Thermodynamical refers to temperature and velocity as drivers of the radiation field anisotropy.

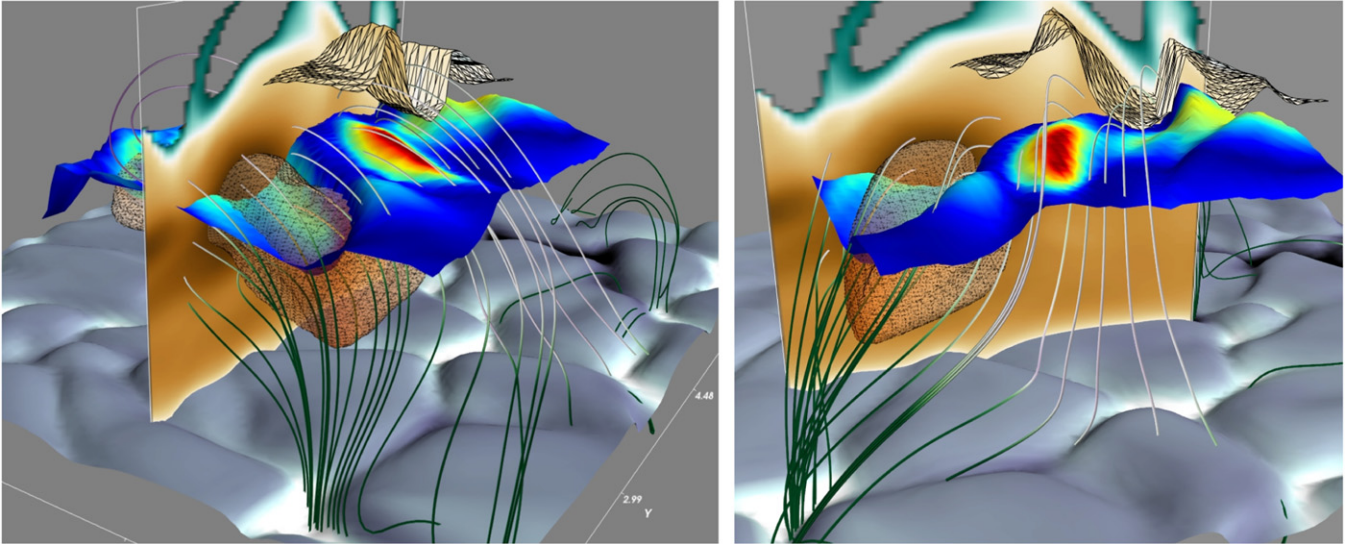


Figure 6. Visualization of a chromospheric “cool bubble” (semitransparent dotted volume). The vertical plane shows the temperature variation (darker brown is cooler). The corrugated surface sketched with polygons traces the heights where $\tau_{v_0} = 1$ for the K line. The colored corrugated surface traces the heights where $\tau_{8542} = 1$ and its color represents the emergent Q/I in the 8542 Å line (darker blue means smaller Q/I). The height of the formation layer goes down inside the cool volume. In the borders of the region, the linear polarization vanishes, therefore drawing a thermodynamic HPIL. This is favored by the illumination of the K line from upper layers (polygonal surface) and by the very different kinematic and thermodynamic stratifications inside and outside the bubble.

However, some detailed calculations suggest that these structures of null polarization can be effectively distinguished in Ca II IR triplet lines using forthcoming solar facilities (Solar-C, ATST, and Zimpol 3+EST).

5.2. Magnetic Field Intensity Along HPILs

Though the linearly polarized signals are in Hanle saturation, we show in the following that the magnetic field intensity in the models can still be determined using the longitudinal Zeeman effect along the Van Vleck HPILs.

In the weak-field regime, the Zeeman splitting ($\bar{g}\Delta\lambda_B$, with \bar{g} being the effective Landé factor¹²) is small in comparison with the thermal width ($\Delta\lambda_D$) of the line profiles:

$$\bar{g} \cdot \frac{\Delta\lambda_B}{\Delta\lambda_D} = \bar{g} \cdot \frac{1.4 \times 10^{-7} \lambda_0 [\text{Å}] B [G]}{\sqrt{1.663 \times 10^{-2} \frac{T[K]}{m[\text{a.m.u.}] + v_{\text{micro}}^2 [\text{km}^2 \text{ s}^{-2}]}} \ll 1, \quad (4)$$

where $m = 40.06$ a.m.u. (atomic mass units) for calcium, λ_0 is the line center wavelength, v_{micro} is the microturbulent velocity, and the square brackets enclose the corresponding units. In our calculations the condition (4) is always fulfilled across the formation region of the spectral lines. In the absence of atomic orientation and with a constant longitudinal magnetic field component along the formation region, Stokes V in the weak-field regime is analytically approximated by

$$V(\lambda) = -\bar{g} \Delta\lambda_B \cos \theta_B \frac{\partial I(\lambda)}{\partial \lambda}, \quad (5)$$

where θ_B is the inclination of the magnetic field with respect to the LOS in a disk-center observation¹³, and $I(\lambda)$ is the spectral profile of the emergent intensity. Since $\Delta\lambda_B$ is linear in B , Stokes

V is proportional to the longitudinal component of the magnetic field. Then, knowing the magnetic inclination we can obtain the full magnetic field intensity.

To solve for the inclination we have identified the Van Vleck HPILs (Section 5) in the linear polarization maps. In a hypothetical real observation such discrimination is more easily done in the maps of the *total* linear polarization after integrating it around line center in order to improve the contrast between pixels in and out of the HPILs. As the Van Vleck HPILs are located where $\theta_B = 54^\circ.73$ at $\tau_{v_0} = 1$, the magnetic field strength B at $\tau_{v_0} = 1$ is estimated from Equation (5) as

$$B [G] = 3.71 \times 10^{12} \frac{|V(\lambda_{\text{core}})|}{\bar{g} \lambda_0^2 \left| \frac{\partial I(\lambda)}{\partial \lambda} \right|_{\lambda=\lambda_{\text{core}}}}, \quad (6)$$

with wavelengths in angstrom units. The ratio between the derivative of the intensity and Stokes V is wavelength dependent. For each pixel, we adaptively chose the points in a small bandwidth λ_{core} aside from the line core of the Stokes V profile without taking the points in and around the peaks of the signal. We calculated the ratio appearing in Equation (6), evaluating it in all the selected wavelength points and fitting it to a straight line, using its slope as the sought result.

The magnetic field strengths resulting from the calculation along the five Van Vleck HPILs found for the Ca II 8542 Å line are shown in the left panel of Figure 7. Pixels where temperature and velocity gradients are larger present larger (but not large) discrepancies between estimated and real magnetic field intensities. The comparison shows that the spectral lines are formed in the weak field regime because Equation (5) effectively allows us to recover the original magnetic field in the models, despite the small deviations owing to dynamics.

One could argue that the circular polarization produced by the longitudinal Zeeman effect in the Ca II 8542 Å line is of limited application for diagnosing the chromospheric magnetism because the response function of Stokes V is only significant from the lower chromosphere downward (Uitenbroek 2006). However, we find that a correct inference of the magnetic

¹² The Ca II IR triplet lines have $\bar{g}_{8498} = 1.06$, $\bar{g}_{8662} = 0.83$, and $\bar{g}_{8542} = 1.1$.

¹³ Away from disk center, the cosine of the angle between the LOS and the magnetic field vector would not be $\cos \theta_B$ but $\cos \theta_B \cos \theta + \sin \theta_B \sin \theta \cos(\chi - \chi_B)$.

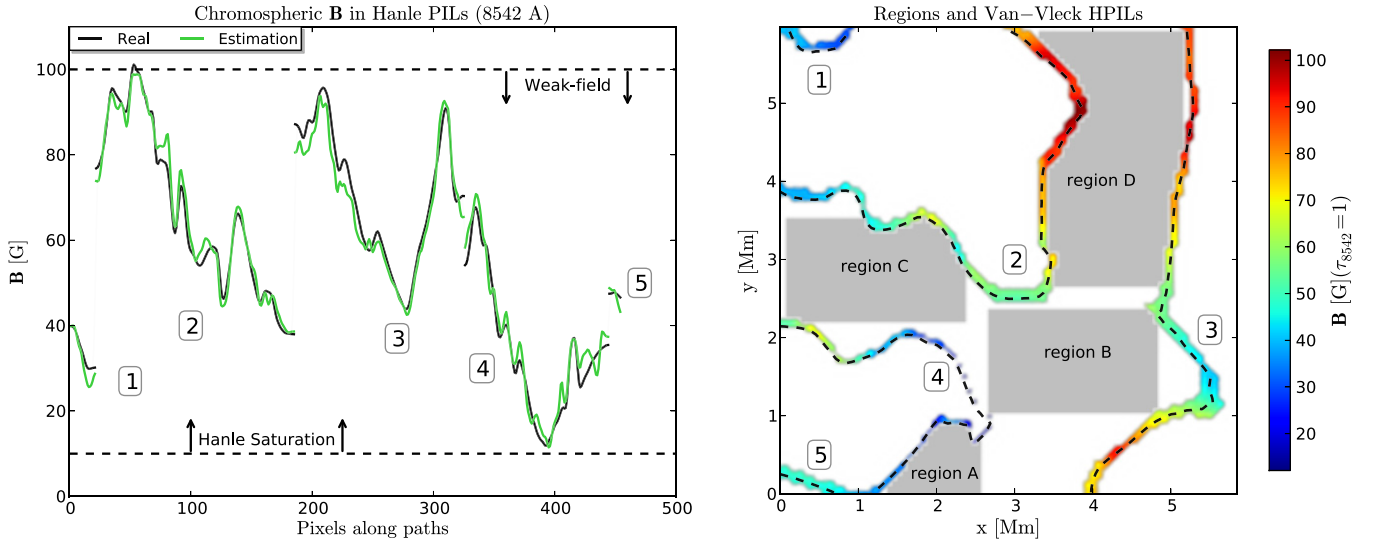


Figure 7. Left: comparison between the real and the estimated chromospheric magnetic field intensity (at $\tau_{8542} = 1$) in the pixels defining the Van Vleck HPILs. Right: the colored lines are the Van Vleck HPILs obtained from Stokes Q and U , the colors representing the chromospheric magnetic field intensity. The gray regions contain the pixels considered for making the Hanle diagrams of Figure 8.

field in the bulk of the medium chromosphere seems possible when evaluating Equation (6) as explained above: including some wavelengths in the footpoints of the Stokes V lobes but avoiding the peaks. Remarkably, as those footpoints are more robust to noise than the very core, they serve well for anchoring the slope of the ratio in Equation (6) when it is calculated with a linear fit. On the contrary, selecting wavelengths in the Stokes V peaks, the magnetic field strength delivered by Equation (6) effectively corresponds to deeper layers, as expected. A similar restriction to core wavelengths has been used by Wöger et al. (2009) when applying the Hybrid Bisector-COG method to quiet Sun observations of Ca II 8542.

6. DYNAMIC SIGNATURES IN HANLE DIAGRAMS

The dependency of the scattering polarization signals on the radiation field anisotropy and solar kinematics/thermodynamics suggests the advantage of using Hanle diagrams for studying the dynamic evolution of the chromosphere jointly with its magnetic field. The development of diagnostic metrics based on such diagrams requires understanding the signatures produced by the chromospheric dynamic events. Next, we use “dynamic” Hanle diagrams to elaborate on this purpose and to establish a basis for deeper developments.

We studied the synthetic Hanle diagrams for the 8542 Å and Ca II K lines (Figure 8, lower and upper panels, respectively) in four regions of our maps. For comparison, a suitable reference for the 8542 Å Hanle diagrams in (non-dynamic) FALC models and forward-scattering can be found in Figures 14 and 15 of Manso Sainz & Trujillo Bueno (2010). The four spatial regions selected in our maps are labeled A, B, C, and D in the right panel of Figure 7, all of them being in the HF region. The small Region A has an expanding chromosphere with significant velocity. Region B is a cool area with patches in different states of motion: static, upward, and downward (having strong downflows). Region C contains a cool bubble with downward velocities and an elongated portion with expanding hot plasma. Finally, region D is the largest, hottest, and has the strongest magnetic field. Each small circle in the Hanle diagrams corresponds to one pixel of the spatial map, and their

colors encode the values of the vertical velocity at $\tau_{v_0} = 1$. The correspondence between the position of each pixel in the map and the position of each pixel in the Hanle diagram can be easily followed in synthetic (and observational) maps. Different small-scale structures of the quiet Sun can thus be studied as different curves and shapes in the Hanle diagram, with the advantage that the axes of the Hanle diagram have associated a physical meaning encoding anisotropy, magnetic field, and dynamics.

Using the approximate Equations (1), we can understand the Hanle diagrams for the 8542 Å line (Figure 8) as curves in polar coordinates. The corresponding radius r of a given point depends on the inclination of the magnetic field and on the thermodynamic factor \mathcal{F} , but with no dependence on the field strength because the IR triplet is Hanle saturated:

$$\left(\frac{Q}{I}\right) = r(\mathcal{F}, \theta_B) \cdot \cos 2\chi_B, \quad (7a)$$

$$\left(\frac{U}{I}\right) = r(\mathcal{F}, \theta_B) \cdot \sin 2\chi_B. \quad (7b)$$

As the points drawn in the bottom panels of Figure 8 for the 8542 Å line correspond to the same pixels in the spatial maps as the points in the upper row, the whole figure illustrates the effect of changing from a *mid-chromosphere* line to a *top chromosphere* line in the (Q, U) space. In the case of the K line, the assumption of saturation in the Hanle effect is in principle not valid, on one hand because this line forms at top chromospheric layers, where the magnetic field intensity is reduced (compared to lower layers); on the other hand, because the intrinsic critical Hanle field of the upper level of the K line is large enough, typical of resonant lines with large emission coefficients A_{ul} . In that case, the polar radius of a given point in the Hanle diagram depends also on the magnetic field strength.

However, there is no observational rule for knowing which areas of a Hanle polarization map are effectively saturated. Our analysis suggest that the signature of the sensitivity to the magnetic field strength in the K line appears in Figure 8 (bottom-row panels) as a general absence of order when connecting adjacent points. On the contrary, a close inspection of the 8542 Å

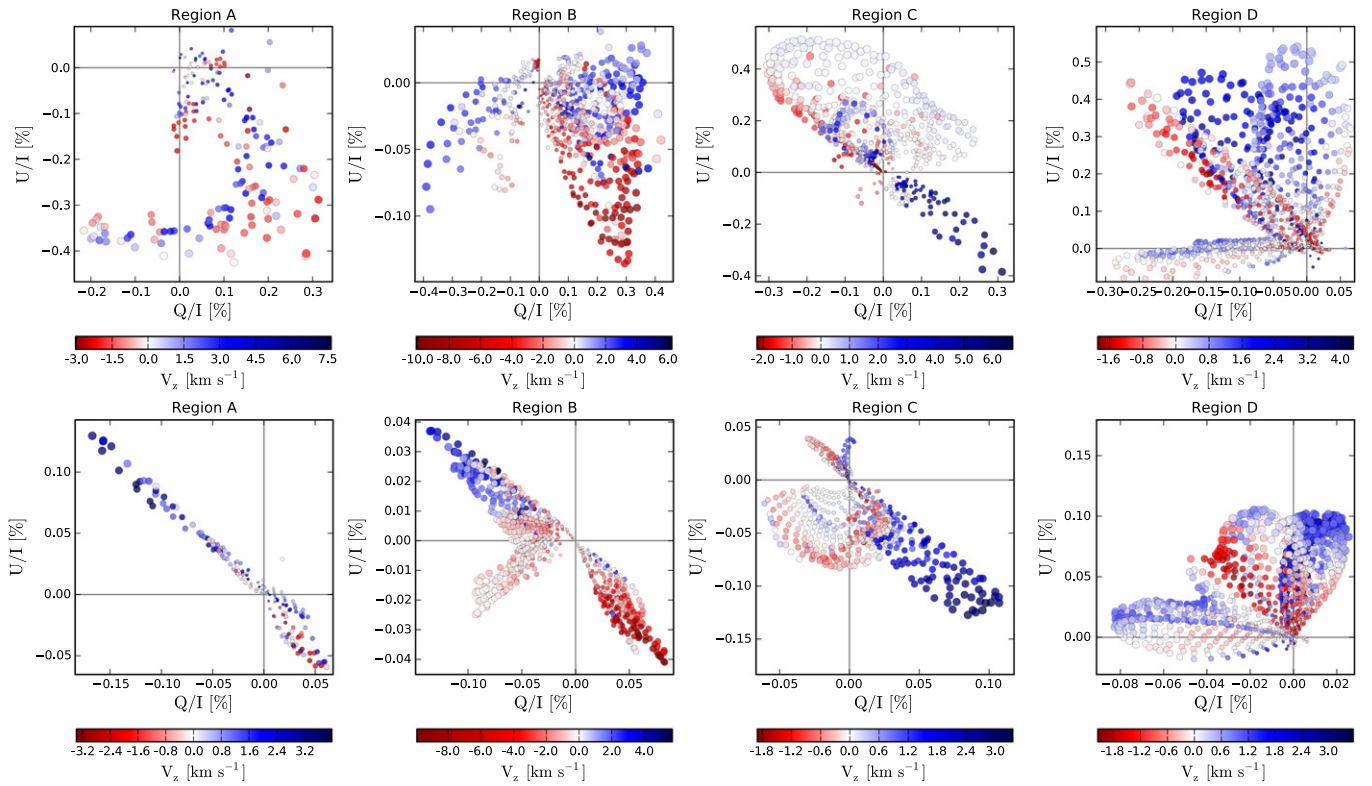


Figure 8. Forward scattering Hanle diagrams in the selected regions of Figure 7 for the 3934 Å and the 8542 Å lines (top and bottom panels, respectively). Each small circle is slightly semitransparent and represents a pixel in the corresponding region. The color encodes the value of the vertical velocity (at the height of formation of the corresponding line) and the size of each circle is proportional to the distance to the axes' origin.

diagrams shows that their points are *generally* aligned following organized trajectories. In general, those trajectories can be fit without needing changes in the magnetic field strength, only with continuous variations of the magnetic field orientation across the selected spatial regions in the maps.

There are, however, notable exceptions in the 8542 Å diagrams that suggest a clear lack of order (examples are the darkest red points in regions B and D). The source of such exceptions in the 8542 Å diagrams is dynamics: modulation of the scattering polarization signals by velocity and temperature shocks crossing the chromosphere. As the horizontal variations in temperature and velocity are comparatively larger and mostly occur in shorter spatial scales than the ones in magnetic field orientation, the radial variations between (Q, U) points corresponding to adjacent pixels can be significantly enlarged while their corresponding azimuthal displacement cannot. Thus, the radial excursions adding some disorder to the diagrams of the 8542 Å line are typical signatures of dynamic effects. As sudden radial variations can be distinguished from azimuthal ones, we have here a possible proxy for discriminating between the action of the magnetic field and the kinematic.

Although the dynamic modulation is also present in the K line core, the effect is not so strong because the ratio between the Doppler shifts and the thermal broadening of the absorption profiles in the top chromosphere is not as large as in the formation region of the 8542 Å line, in such a way that the action of the velocity gradients on the anisotropy of the radiation field is reduced (Carlin et al. 2012). Furthermore, the action of the magnetic intensity on the K line polarization could also be to spread out the points in azimuth, thus contributing to diluting the strong radial excursions. We cannot confirm this

from Equations (1) because they are valid for Hanle-saturated lines.

A similar analysis can be carried out using local temperature instead of velocity. We find correlations between points with larger temperatures, larger velocities, and larger Q and U signals for the 8542 Å line. All suggest the picture of a quiet chromosphere where the Hanle-saturated signals of the 8542 Å line mapping the magnetic field orientation are abruptly modified by the dynamic effects associated with the propagation of shocks.

The atmospheric model employed here has larger resolution and reduced kinematics compared to the real observed Sun, which suggests that the dynamic effects above could be significantly stronger. The improvements in resolution, both in synthetic models and in observational maps, will transform the sub-pixel (now microturbulent) kinematic into macroscopic velocities, thus making the effects presented in this paper increasingly more evident and relevant for reproducing the observations.

7. CONCLUSIONS

A better understanding of the forward-scattering polarization signals requires 2D spectropolarimetry for measuring polarization maps instead of slit profiles. Magnetic field diagnosis at (or near) forward-scattering shows several unexploited advantages: first, although the forward-scattering signals have lower amplitude because the level of polarization produced by solar curvature is naturally removed at disk center, the number of collected photons is significantly increased with respect to the limb (limb darkening); second, the forward scattering Hanle

effect generates Q and U signals having similar amplitudes and reacting similarly to the B inclination; third, in contraposition to slit-like observations, the spatial continuity in the maps provides important help for understanding the magnetic topology and discriminating the magnetic and kinematic contributions to the linear polarization signals; fourth, PRD effects in the scattering process are minimized at disk center, which suppresses polarized emission in the spectral wings; and fifth, as the effects of the solar curvature and PRD in the linear polarization are avoided, the corresponding profiles at disk center are “purer”. They are driven by magnetic field (the Hanle effect) and solar dynamics (through the radiation field anisotropy).

Thus, the fundamental point is the discrimination between the Hanle and dynamic effects, because both modulate the line-core polarization (independently, in principle). Such discrimination is possible by understanding the variability and the characteristics of the polarization signals in wavelength (Carlin et al. 2012), time (Carlin et al. 2013), and space (this paper) from realistic atmospheric models. Analyzing jointly the Stokes vector spectrum, the spatial information in the polarization maps and the atmosphere model, we have outlined the expected behavior of the chromospheric Ca II lines in a quiet Sun context. We conclude that the combination of the forward-scattering Hanle effect with temperature and velocity dynamics should produce characteristic spatial patterns in the linear polarization signals of spectral lines forming at the solar chromosphere. When these signals are synthesized in MHD models we find that the Hanle effect operates in saturation for the Ca II IR triplet. With the aid of analytical formulas derived for this physical situation, we have introduced the concept of Hanle polarity inversion line, defining and explaining three types of spatial signatures: azimuthal, Van Vleck, and thermodynamical. The so-called thermodynamical HPILs can offer new diagnostic metrics to identify very particular dynamical situations in the atmosphere, like the one confining cool volumes of chromospheric plasma. The other kinds of HPILs found in our synthetic maps encode the orientation of the chromospheric magnetic field, representing a precious magnetic fingerprint of the chromosphere.

Using the Stokes V profiles, we have shown how the Van Vleck HPILs could serve to infer the chromospheric magnetic field strength along themselves. Hence, the detection of HPILs is not only a direct measurement of the magnetic field orientation but also an interesting constraint for the magnetic field strength. This discussion suggests a question: Having a high-resolution and high-sensitivity polarization map at disk center, can we obtain a precise map of the magnetic field using the spatial locations where the polarization amplitudes *cancel out*?

Our results should be tested observationally with chromospheric spectral lines and instrumentation providing good signal-to-noise ratios with enough spatial resolution. The extension of this work to the full 3D RT case will quantify whether the horizontal inhomogeneities of the plasma can mask the location of the HPILs or smooth their contrast significantly.

In this paper we have also calculated synthetic Hanle diagrams characterizing a dynamic chromosphere in presence of magnetic field. The spatial and temporal evolution of the points in such diagrams translates the physical problem of the diagnostic to a more suitable representation and suggests that the variations of magnetic field and temperature/velocity could be studied and understood jointly. On one hand, the signatures of an amplitude modulation produced by vertical gradients of velocity and temperature are abrupt radial excursions of the points in the Hanle diagram. On the other hand, points that follow ordered

curved trajectories in the diagrams seem to indicate Hanle saturation in the corresponding region of the spatial maps. Their variations are guided by magnetic field azimuth and inclination. On the contrary, when the Hanle effect is not saturated, the polarization points cannot be easily ascribed to a parametric curve because the action of the magnetic field intensity spreads them out in a more chaotic way across the (Q, U) space. Provided that the noise uncertainties do not exceed a certain threshold, this idea can serve to easily diagnose Hanle saturation in regions of the solar surface.

We thank Javier Trujillo Bueno and Rafael Manso Sainz for helpful discussions and advice and Mats Carlsson and J. Leenaarts for providing us with the atmospheric models. E.S.C. gratefully acknowledges the financial support given by the Istituto Ricerche Solari Locarno (IRSOL) through the State Secretariat for Education, Research, and Innovation (SERI, Canton Ticino), the COST project C12.0084, and the municipalities affiliated with CISL and the Aldo e Cele Daccò Foundation as well as by the Instituto de Astrofísica de Canarias through the Resident Astrophysicist fellowship. Financial support by the Spanish Ministry of Economy and Competitiveness through projects AYA2010–18029 (Solar Magnetism and Astrophysical Spectropolarimetry) and Consolider-Ingenio 2010 CSD2009–00038 is also gratefully acknowledged. A.A.R. acknowledges financial support through the Ramón y Cajal fellowships.

APPENDIX THE RT CODE

Traviata is a multilevel RT code for the synthesis of the spectral line polarization resulting from atomic polarization and the Hanle effect in weakly magnetized stellar atmospheres (Manso Sainz & Trujillo Bueno 2003b, 2010). Essentially, it solves the RT problem of the second kind in the framework of the quantum theory of spectral line polarization under the flat-spectrum approximation. Quantum coherences and population imbalances between magnetic energy sublevels of any given J level are considered. We have added new functionalities to this code. Namely:

1. Effect of vertical (non-relativistic) velocities in the RT and in the Statistical Equilibrium Equations.

The calculation is posed and solved in an external observer’s reference frame, to which all the motions in the plasma are related. The absorption, emission, and dispersion coefficients depend on position, frequency, spectral transition, and, due to the velocity, on the inclination of the rays of the angular quadrature. Upward velocities give blue shifts in the spectral profiles.

2. Adaptive numerical grids.

For each column of the model, a symmetric frequency axis is created, having a variable adaptive resolution to correctly sample the Doppler-induced features along the Stokes profiles. Initially, it is calculated for each vertical considering the existing maximum velocity and remains fixed thereafter. Angular and spatial numerical grids are heavily restricted by the presence of velocities due to the maximum Doppler shift at each column. For a good spectral sampling, the change in Doppler velocity $\Delta(\mu_k V_i) = \Delta\mu_k \cdot V_i + \Delta V_i \cdot \mu_k$ in the spatial and angular grid has to be small enough (i.e., of the order of half Doppler width) between adjacent points along the same ray k and also between

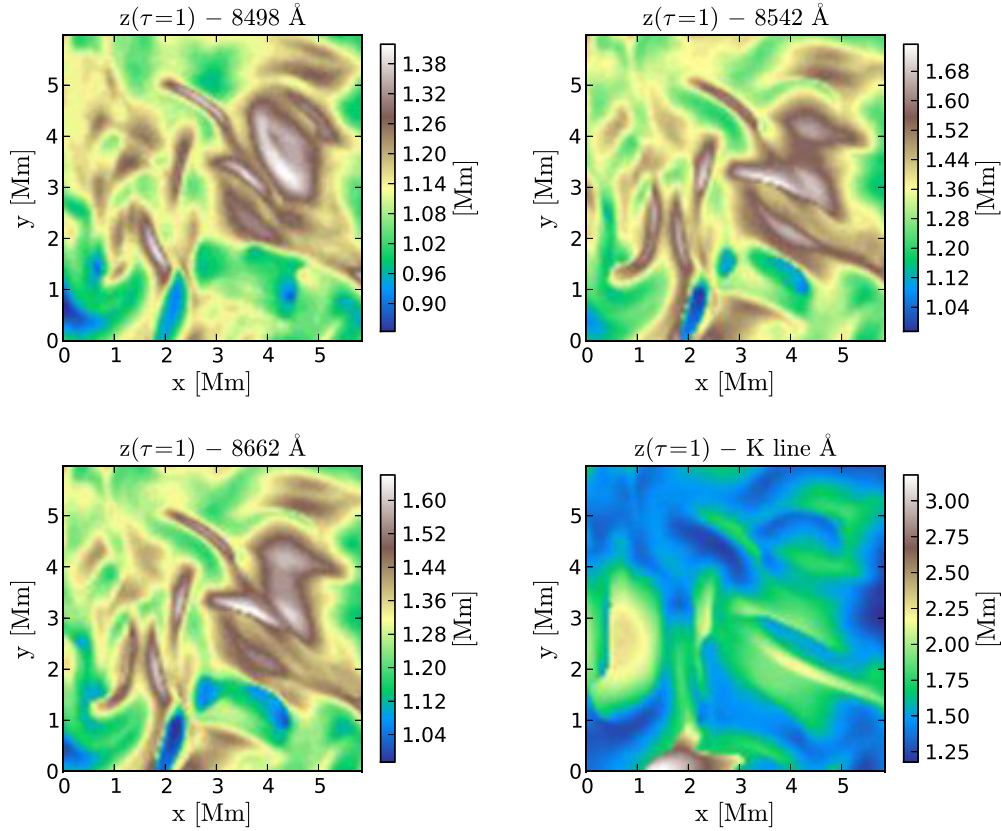


Figure A1. Heights of $\tau_{v_0} = 1$ for the spectral lines under consideration. We can use the K line picture to identify expanded or compressed atmospheres because there is a correlation between this feature and the heights where the K line optical depth is unity.

adjacent points along the same height i . On one hand, this constrains the angular grid to fulfill $|\Delta\mu_{\max} V_{\max}| \lesssim \frac{1}{2}$, where $\Delta\mu_{\max}$ gives the maximum allowed angular step in the quadrature. On the other hand, the spatial grid is constrained by $\Delta V_i = |V_i - V_{i-1}| \lesssim 1/2$, which limits the maximum Doppler velocity gradient between two adjacent layers i and $i - 1$ in the atmosphere.

3. Variation of all the quantities with height.
4. Calculation of Stokes V in the Zeeman regime.

The code uses the total level populations to solve the Zeeman transfer equation for I and V along the observer LOS:

$$\frac{d}{ds} \begin{pmatrix} I \\ V \end{pmatrix} = \begin{pmatrix} \epsilon_I \\ \epsilon_V \end{pmatrix} - \begin{pmatrix} \eta_I & \eta_V \\ \eta_V & \eta_I \end{pmatrix} \begin{pmatrix} I \\ V \end{pmatrix}. \quad (\text{A1})$$

The dispersion (magneto-optical) terms are neglected when calculating Stokes V because their contributions are insignificant in weakly magnetized atmospheres for this Stokes parameter. To solve the system of equations, we transform it in two independent equations:

$$\frac{d}{ds} \begin{pmatrix} I^+ \\ I^- \end{pmatrix} = \begin{pmatrix} \epsilon^+ \\ \epsilon^- \end{pmatrix} - \begin{pmatrix} \eta^+ I^+ \\ \eta^- I^- \end{pmatrix}, \quad (\text{A2})$$

creating the variables $I^\pm = I \pm V$, $\epsilon^\pm = \epsilon_I \pm \epsilon_V$ and $\eta^\pm = \eta_I \pm \eta_V$. Both equations are solved along the LOS using a parabolic short-characteristic method to obtain the emergent I^+ and I^- profiles for each frequency and spectral transition. The solution for the original variables is then obtained with $I = (I^+ + I^-)/2$ and $V = (I^+ - I^-)/2$.

The Stokes V line radiative coefficients (absorption and emission terms) are calculated without atomic orientation, following the standard expressions for the longitudinal Zeeman effect (e.g., Landi Degl'Innocenti & Landolfi 2004; Stenflo 1994). Namely, the line emissivity is

$$\epsilon_V^l(v, \mathbf{\Omega}) = (h\nu/4\pi) A_{u\ell} N_u \phi_V(v, \mathbf{\Omega}), \quad (\text{A3})$$

with

$$\phi_V(v, \mathbf{\Omega}) = \frac{1}{2} [\phi_1 - \phi_{-1}] \cos \hat{\theta} \quad (\text{A4})$$

and

$$\phi_q = \sum_{M_\ell M_u} 3 \begin{pmatrix} J_u & J_\ell & 1 \\ -M_u & M_\ell & -q \end{pmatrix}^2 \phi(v - \nu_{J_u M_u, J_\ell M_\ell}) \times (q = -1, 0, -1) \quad (\text{A5})$$

describing the superposition of Zeeman components $\phi(v - \nu_{J_u M_u, J_\ell M_\ell})$, which are evaluated around its corresponding Zeeman frequency $\nu_{J_u M_u, J_\ell M_\ell} = \nu_0 + \nu_L(g_u M_u - g_\ell M_\ell)$. For each transition, $u \leftrightarrow \ell$, $A_{u\ell}$ is the Einstein coefficient for spontaneous emission and N_u is the total population of the upper level per unit volume. Note also that $\hat{\theta}$ is the direct angle between the local magnetic field vector and the direction $\mathbf{\Omega}$ of a given ray light passing through the considered plasma element. Working in the reference frame of the solar vertical, this angle can be calculated locally at every point in the atmosphere with

$$\cos \hat{\theta} = \cos \theta \cos \theta_B + \sin \theta \sin \theta_B \cos(\chi_B - \chi), \quad (\text{A6})$$

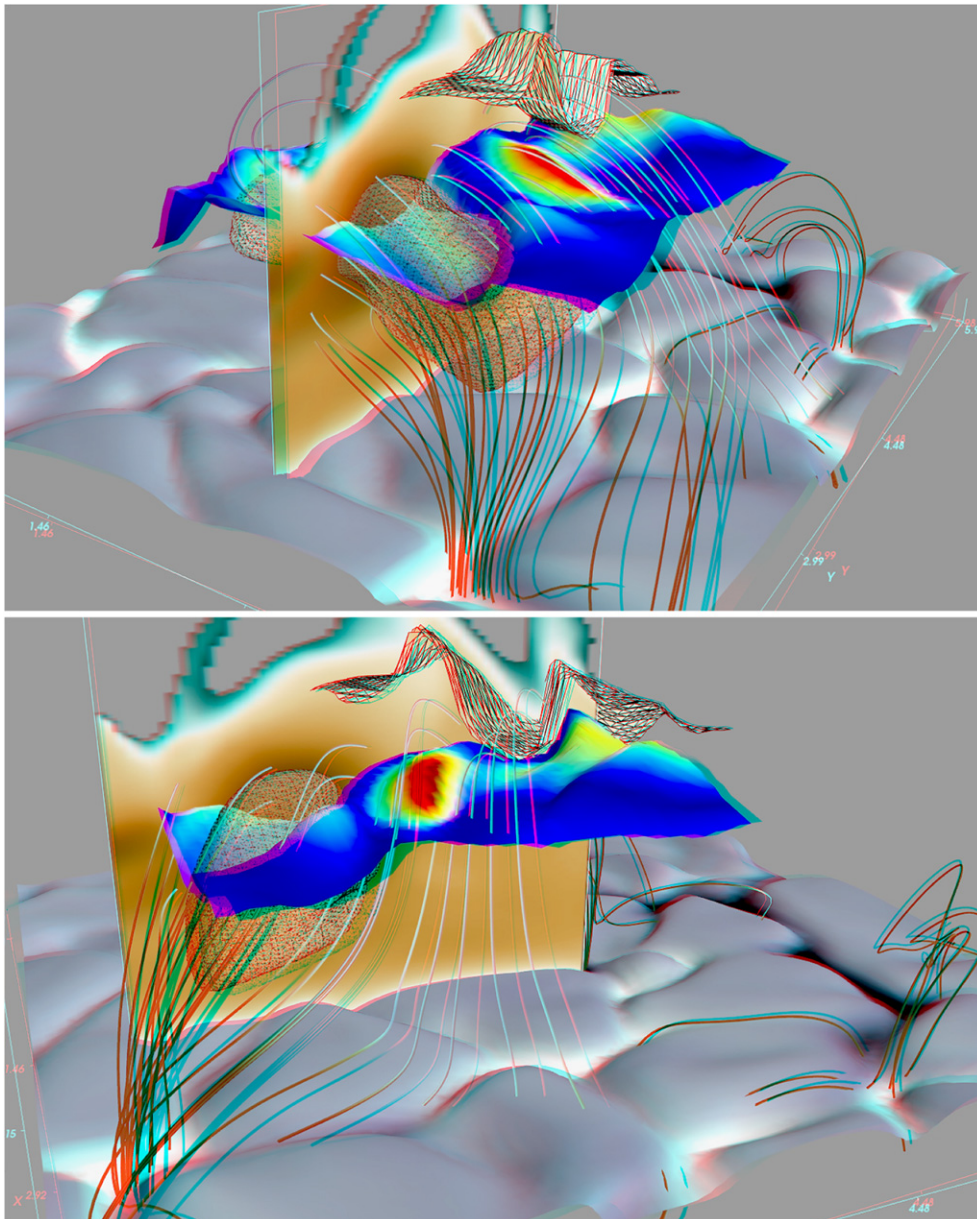


Figure A2. Similar to Figure 6 but in a stereographic representation. Cyan–red glasses are required to see this figures correctly.

being the θ and χ the angles defining the direction of the ray in such reference system.

5. Automation and parallelization for working with large atmospheric models. The processing of the atmospheric model includes interpolation of the physical magnitudes in grid intervals with large gradients, initialization with atomic populations obtained in near positions in the data set and management and re-processing of models with convergence problems, which have to be recomputed with another interpolation grid, with other parameter settings or with other initializing populations. To accelerate the convergence, we have implemented an OpenMP parallelization on the RT loop.

As a result, the code can treat large atmospheric data sets, considering vertical gradients in all the physical quantities and obtaining the LP signals produced by scattering and the Hanle effect and the circular polarization produced by the Zeeman effect.

REFERENCES

- Anusha, L. S., & Nagendra, K. N. 2011, *ApJ*, **738**, 116
- Anusha, L. S., Nagendra, K. N., Bianda, M., et al. 2011, *ApJ*, **737**, 95
- Asensio Ramos, A. 2004, PhD thesis, Universidad de La Laguna, La Laguna
- Asensio Ramos, A. 2014, *A&A*, **563**, A114
- Bianda, M., Ramelli, R., Anusha, L. S., et al. 2011, *A&A*, **530**, L13
- Bommier, V. 1997, *A&A*, **328**, 726
- Carlin, E. S., Asensio Ramos, A., & Trujillo Bueno, J. 2013, *ApJ*, **764**, 40
- Carlin, E. S., Manso Sainz, R., Asensio Ramos, A., & Trujillo Bueno, J. 2012, *ApJ*, **751**, 5
- Casini, R., Landi Degl'Innocenti, M., Manso Sainz, R., Landi Degl'Innocenti, E., & Landolfi, M. 2014, *ApJ*, **791**, 94
- de la Cruz Rodríguez, J., De Pontieu, B., Carlsson, M., & Rouppe van der Voort, L. H. M. 2013, *ApJL*, **764**, L11
- De la Cruz Rodríguez, J., Socas-Navarro, H., Carlsson, M., & Leenaarts, J. 2012, *A&A*, **543**, 34
- Derouich, M., Trujillo Bueno, J., & Manso Sainz, R. 2007, *A&A*, **472**, 269
- Hansteen, V. H., Carlsson, M., & Gudiksen, B. 2007, in *ASP Conf. Ser.* 368, *The Physics of Chromospheric Plasmas*, ed. P. Heinzel, I. Dorotovič, & R. J. Rutten (San Francisco, CA: ASP), 107
- Jefferies, J., Lites, B. W., & Skumanich, A. 1989, *ApJ*, **343**, 920

- Judge, P., Knölker, M., Schmidt, W., & Steiner, O. 2010, *ApJ*, **720**, 776
- Khomenko, E., & Collados, M. 2012, *ApJ*, **747**, 87
- Landi Degl'Innocenti, E. 1984, *SoPh*, **91**, 1
- Landi Degl'Innocenti, E., & Landi Degl'Innocenti, M. 1973, *SoPh*, **31**, 299
- Landi Degl'Innocenti, E., & Landolfi, M. 2004, *Polarization in Spectral Lines* (Dordrecht: Kluwer)
- Leenaarts, J., Carlsson, M., Hansteen, V., & Rouppe van der Voort, L. 2009, *ApJL*, **694**, L128
- Linsky, J. L., & Avrett, E. H. 1970, *PASP*, **82**, 169
- Manso Sainz, R., & Trujillo Bueno, J. 2003a, *PhRvL*, **91**, 111102
- Manso Sainz, R., & Trujillo Bueno, J. 2003b, in ASP Conf. Ser. 307, *Solar Polarization*, ed. J. Trujillo-Bueno & J. Sanchez Almeida (San Francisco, CA: ASP), **251**
- Manso Sainz, R., & Trujillo Bueno, J. 2010, *ApJ*, **722**, 1416
- Martínez Pillet, V., García López, R. J., del Toro Iniesta, J. C., et al. 1990, *ApJL*, **361**, L81
- Martínez-Sykora, J., De Pontieu, B., & Hansteen, V. 2012, *ApJ*, **753**, 161
- Mihalas, D. 1978, *Stellar Atmospheres* (San Francisco, CA: W. H. Freeman and Co.)
- Pietarila, A., Socas-Navarro, H., & Bogdan, T. 2007, *ApJ*, **670**, 885
- Reardon, K., Tritschler, A., & Katsukawa, Y. 2013, *ApJ*, **779**, 143
- Shine, R. A., & Linsky, J. L. 1974, *SoPh*, **39**, 49
- Socas-Navarro, H., Elmore, D., Pietarila, A., et al. 2006, *SoPh*, **235**, 55
- Stenflo, J. O. 1994, *Solar Magnetic Fields. Polarized Radiation Diagnostics* (Dordrecht: Kluwer)
- Stenflo, J. O. 2003, in ASP Conf. Ser. 307, *Solar Polarization 3*, ed. J. Trujillo Bueno & J. Sánchez Almeida (San Francisco, CA: ASP), **385**
- Stenflo, J. O. 2006, in ASP Conf. Ser. 358, *Solar Polarization 4*, ed. R. Casini & B. W. Lites (San Francisco, CA: ASP), **215**
- Stenflo, J. O., & Keller, C. U. 1997, *A&A*, **321**, 927
- Štěpán, J., & Trujillo Bueno, J. 2013, *A&A*, **557**, A143
- Trujillo Bueno, J. 2003a, in ASP Conf. Proc. 288, *Stellar Atmosphere Modeling*, ed. I. Hubeny, D. Mihalas, & K. Werner (San Francisco, CA: ASP), **511**
- Trujillo Bueno, J. 2003b, in ASP Conf. Ser. 307, *Solar Polarization*, ed. J. Trujillo-Bueno & J. Sanchez Almeida (San Francisco, CA: ASP), **407**
- Trujillo Bueno, J., Landi Degl'Innocenti, E., Collados, M., Merenda, L., & Manso Sainz, R. 2002, *Natur*, **415**, 403
- Trujillo Bueno, J., & Manso Sainz, R. 1999, *ApJ*, **516**, 436
- Trujillo Bueno, J., Shchukina, N., & Asensio Ramos, A. 2004, *Natur*, **430**, 326
- Uitenbroek, H. 1989, *A&A*, **213**, 360
- Uitenbroek, H. 2006, in ASP Conf. Ser. 354, *Solar MHD Theory and Observations: A High Spatial Resolution Perspective*, ed. J. Leibacher, R. F. Stein, & H. Uitenbroek (San Francisco, CA: ASP), **313**
- Wöger, F., Wedemeyer-Böhm, S., Uitenbroek, H., & Rimmele, T. R. 2009, *ApJ*, **706**, 148